The first high-resolution tropospheric NO_2 observations from the Ultraviolet Visible Hyperspectral Imaing Spectrometer (UVHIS)

Liang Xi [1,2], Fuqi Si [1], Yu Jiang [1], Haijin Zhou [1], Kai Zhan [1], Zhen Chang [1], Xiaohan Qiu [1] and Dongshang Yang [1,2]

[1]Key Laboratory of Environmental Optics and Technology, Anhui Institute of Optics and Fine Mechanics, Chinese Academy of Sciences, Hefei 230031, China
[2] University of Science and Technology of China, Hefei, 230026, Anhui, China

Correspondence to: Fuqi Si (sifuqi@aiofm.ac.cn)

Abstract. We present a novel airborne imaging differential optical absorption spectroscopy (DOAS) instrument: Ultraviolet Visible Hyperspectral Imaging Spectrometer (UVHIS), which is developed for trace gas monitoring and pollution mapping. Within a broad spectral range from 200 to 500 nm, operated in three channels, the spectral resolution of UVHIS is better than 0.5 nm. The optical design of each channel comprises a fore-optics with a field of view (FOV) of 40°, an Offner imaging spectrometer, and a charge-coupled device (CCD) array detector of 1032×1072 pixels. A first demonstration flight using UVHIS was undertaken on 23 June 2018, above an approximate 600 km^2 area in Feicheng, China, with a spatial resolution of about 25×22 m^2. Measurements of nadir backscattered solar radiation of channel 3 are used to retrieve tropospheric vertical column densities (VCDs) of NO_2 with a mean total error of 3.0×10^{15} molec cm^{-2}. The UVHIS instrument clearly detected several emission plumes transporting from south to north, with a peak value of 3×10^{16} molec cm^{-2} in the dominant one. UVHIS NO_2 vertical columns are well correlated with ground-based mobile DOAS observations, with a correlation coefficient of 0.65 for all co-located measurements, a correlation coefficient of 0.86 for co-located measurements that only circled the steel factory, and a slight underestimation for polluted observations. This study demonstrates the capability of UVHIS for NO_2 local emission and transmission monitoring.

1 Introduction

Nitrogen oxides (NO_x), the sum of nitrogen monoxide (NO) and nitrogen dioxide (NO_2), plays a key role in the chemistry of the atmosphere, such as the ozone destruction in the stratosphere (Solomon, 1999), and the secondary aerosol formation in the troposphere (Seinfeld and Pandis, 2016). In the troposphere, despite lightning, soil emissions and other natural processes, the main sources of NO_x are anthropogenic activities like fossil fuel combustion by power plants, factories, and road transportation, especially in the urban and polluted regions. As an indicator of anthropogenic pollution which leads to negative effects both on the environment and human health, the amounts and spatial distributions of NO_x attract large attention. For example, China becomes one of the largest NO_x emitters in the world due to fast industrialization, meanwhile China is also experiencing a series of severe air pollution problems in recent years (Crippa et al., 2018; An et al., 2019).

Therefore measuring NO_x distribution by application of different techniques, would benefit the pollutant emission detection and the air quality trend forecast (Liu et al., 2017; Zhang et al., 2019).

Compared to NO, Nitrogen dioxide (NO_2) is more stable in the atmosphere. Based on the characteristic absorption structures of NO_2 in the ultraviolet-visible spectral range, the differential optical absorption spectroscopy (DOAS) technique has been applied to retrieve the light path integrated densities from different platforms (Platt and Stutz, 2008). Combining the imaging spectroscopy technique, imaging DOAS instruments were developed in recent years to determine the trace gases temporal variation as well as the two dimensional distribution. Global horizontal distribution of tropospheric NO_2 and other trace gases has been mapped and studied by several space-borne sensors, including SCIAMACHY (Scanning Imaging Absorption Spectrometer for Atmospheric CHartographY; Bovensmann et al., 1999), GOME (Global Ozone Monitoring Experiment; Burrows et al., 1999), GOME-2 (Munro et al., 2016), OMI (Ozone Monitoring Instrument; Levelt et al., 2006) and TROPOMI (TROpospheric Ozone Monitoring Instrument; Veefkind et al., 2012). The Environmental trace gases Monitoring Instrument (EIM; Zhao et al., 2018; Cheng et al., 2019; Zhang et al., 2020), as the first designed space-borne trace gas sensor in China, was launched on 9 May 2018, on-board the Chinese GaoFen-5 (GF5) satellite. In terms of spatial resolution, the majority of these space-borne sensors are lower than 10×10 km^2, except TROPOMI with a relative higher resolution of 3.5 $\times 5.5$ km^2.

In order to achieve spatial resolution higher than 100×100 m^2 to investigate the spatial distribution in urban areas and individual source emissions, several researchers have applied the imaging DOAS instruments on airborne platforms. The airborne imaging DOAS measurement was firstly performed by Heue et al. (2008) over South African Highveld plateau. For the purpose of retrieval of urban NO_2 horizontal distribution, Popp et al. (2012) and Lawrence et al. (2015) performed their measurements separately in Zürich, Switzerland, and Leicester, England. In 2013, an airborne measurement focusing on source emissions was performed in China, over Tianjin, Tangshan and Bohai gulf (Liu et al., 2015). An inter-comparison study of four airborne imaging DOAS instruments over Berlin, Germany, suggests a good agreement between different sensors, and the effectiveness of imaging DOAS to reveal the fine-scale horizontal variability in tropospheric NO_2 in an urban context (Tack et al., 2019).

Here we present a novel airborne imaging DOAS instrument: Ultraviolet Visible Hyperspectral Imaging Spectrometer (UVHIS), designed and developed by Anhui Institute of Optics and Fine Mechanics, Chinese Academy of Sciences (AIOFM, CAS). As a hyperspectral imaging sensor with high spectral and spatial resolution, UVHIS is designed to be operated on aircraft platform for the purpose of atmospheric trace gas measurements and pollution monitoring over large area in a relative short time frame. By using the DOAS technique and geo-referencing, two dimensional spatial distribution of tropospheric NO_2 of its first demonstration flight over Feicheng, China is also presented in this paper.

The organization of this paper is listed as follows: Sect. 2 presents a technical description of UVHIS system, as well as its preflight calibration results. Section 3 introduces the detailed information of its first research flight above Feicheng, China. Section 4 describes the developed algorithm for retrieval and geographical mapping of tropospheric NO_2 vertical column

densities from hyperspectral data. Section 5 present the retrieved NO_2 column densities, and Section 6 compares airborne measurements with correlative ground-based data sets from a mobile DOAS system.

2 Instrument Details

1.1 The UVHIS instrument

UVHIS is a hyperspectral instrument measuring nadir backscattered solar radiation in the ultraviolet and visible wavelength region from 200 to 500 nm. The instrument is operated in three channels with the wavelength ranges of 200-276 nm (channel 1), 276-380 nm (channel 2) and 380-500 nm (channel 3) for minimal stray light effects and highest spectral performance. The main characteristics of UVHIS are summarized in Table 1.

Figure 1 shows the optical bench of channel 3 and that the other two are similar. The optical design of each channel comprises a telecentric fore-optics, an Offner imaging spectrometer, and a two dimensional charge-coupled device (CCD) array detector. The Offner imaging spectrometer consists of a concave mirror and a convex grating. Backscattered light below the aircraft is collected by a wide-field telescope with a FOV of 40° in the across-track dimension. After passing through a bandpass filter and a 12.5 mm long entrance slit in the focal plane, light is reflected and diffracted by a concave mirror and a convex grating. The dispersed light is imaged onto a frame transfer CCD detector, which consists of 1032 × 1072 individual pixels. For the purpose of alignment and slight adjustment of the spectrometer, only the central 1000 rows of pixel are well illuminated in the across-track dimension. In the wavelength dimension, the image covers central 1024 columns of pixels on the CCD detector while the left and right edge are used to monitor dark current. The spectral sampling and spectral resolution of all three channels can be found in Table 1.

To reduce dark current and improve the signal-to-noise ratio (SNR) of the instrument, the CCD detector is thermally stabilized at −20°C with a temperature stability of ± 0.05°C (Zhang et al., 2017). However, the optical bench is not thermally controlled, because the instrument is mounted inside the aircraft platform which is temperature consistent at 20°C. UVHIS is mounted on a Leica PAV-80 gyro-stabilized platform that provides angular motion compensation. A high-grade Applanix navigation system on-board is used to receive the position (i.e. latitude, longitude, and elevation) and orientation (i.e. pitch, roll, and heading) information, which is required for accurate geo-referencing. The UVHIS instrument telescope collect solar radiation backscattered from the surface and atmosphere through a fused silica window on the bottom of the aircraft. In the case of NO_2 measurement, all observations in this study only use the channel 3.

2.2 Preflight calibration

Spectral and radiometric calibration in the laboratory were done prior to flights to reduce errors in spectral analysis.

For radiometric calibration, we use an integrating sphere with a tungsten halogen lamp for channel 2 and channel 3. While for channel 1, a diffuser plate with a Newport xenon lamp is used for a sufficient ultraviolet output. With the help of a well calibrated spectral radiometer to monitor the radiance of calibration system, digital numbers (DNs) from CCD detectors of

95 three channels can be converted to radiance correctly. Uncertainty of absolute radiance calibration of UVHIS is 4.89 % for channel 1, 4.67 % for channel 2 and 4.42 % for channel 3.

The preflight wavelength calibration was also performed in the laboratory, using a mercury–argon lamp and a tunable laser as light sources. We model the slit function of UVHIS using a symmetric Gaussian function. Spectral registration and slit function calibration are achieved by least square fitting of characteristic lines in collected spectra. Table 2 lists the retrieved

100 full-width at half maximums (FWHMs) for channel 3. Figure 2 shows the measured slit functions at 450.504 nm for 9 viewing angles (-20°, -15°, -10°, -5°, 0°, 5°, 10°, 15°, 20°), and respective retrieved slit function shapes using a symmetric Gaussian function. These Gaussian fit results suggest that a symmetric Gaussian function is a reasonable assumption for slit shape in all viewing directions.

3 Research flight

105 The first demonstration flight above Feicheng city, Shiheng town and neighbouring rural areas was performed on 23 June 2018, aiming at producing tropospheric NO_2 field maps of large area in a relative short time frame. Feicheng is a county-level city in Shandong province, about 410 km away from Beijing. Figure 3 shows the TROPOMI NO_2 tropospheric observation on 23 June, 2018, with the background Google map and the location of Feicheng. The flight area is located on the south bank of the Yellow River, at the western foot of Mount Tai. UVHIS was operated from the Y-5 aircraft at altitude

110 of 3 km above sea level, higher than the height of planetary boundary layer (PBL), with an average aircraft ground speed of 50 m/s. An overview of the observation area and flight lines are provided in Fig. 4. The aircraft took off at local noon from the airfield in Pingyin county, about 19 km northwest of the centre of the field. An area of approximately 600 km^2 was covered in 3 hour, under clean sunny and cloudless conditions with low-speed southerly winds.

Research flight consists of 13 parallel lines in the east-west direction, starting from the lower left corner in Fig. 2. The

115 distance between adjacent lines is 1.5 km, while the swath width of each individual line is about 2.2 km. Gapless coverage between adjacent lines can be guaranteed in this pattern because of the adequate overlap. To validate the NO_2 column densities retrieved from UVHIS by comparison to ground measurements, mobile DOAS measurements were performed inside the research area on the same day. As shown in Fig.4, the measurements of the mobile DOAS system circle around the steel factory and the power plant, which are the presumed major emission sources inside the observation area.

120 In the condition of spatial binning by 10 pixels across-track, the across-track spatial resolution of the ground pixel is about 22 m. At typical aircraft ground speed of 50 m/s and integration time of 0.5 s, the along-track spatial resolution of the ground pixel is about 25 m.

4 Data processing chain

The NO$_2$ tropospheric vertical column density (VCD) retrieval algorithm of UVHIS consists of four major steps. First, some necessary preprocessing procedures are required before any spectral analysis of UVHIS data. Next, UVHIS spectral data after preprocessing are analyzed in a suitable wavelength region by application of the well-established DOAS technique. After that, air mass factors (AMFs) are calculated for every observation based on SCIATRAN radiative transfer model to convert the slant column densities (SCDs) to tropospheric vertical column densities. In the final step, combining with sensor position and orientation information, NO$_2$ VCDs are geo-referenced and overlaid onto Google satellite map layers.

4.1 Preprocessing

The preprocessing procedure before spectral analysis includes data selection, dark current correction, spatial binning, and in-flight calibration. First, the spectral data acquired during U-turns of aircraft are removed in the processing because of the large and changing orientation angles. Also a threshold of radiance values is set to neglect some over-illuminated ground pixels inside the flight area, which are usually caused by presence of cloud or water mirror reflection. During the entire flight, sun glint on water occurred several times in the southern part of flight area, especially above the river near the reference area. However, cloud was not present due to clean clear-sky weather condition.

The dark current correction is performed based on the measurement at the start of the entire flight by blocking the fore-optics, which is necessary to improve instrument performance and reduce analysis error in DOAS fit.

In order to increase the SNR of the instrument and the sensitivity to NO$_2$, the raw pixels of imaging DOAS are usually aggregated in across-track direction and along-track direction. According to photon statistics when only shot noise is considered, the SNR should rise with square root of number of binned spectra. However, this improved SNR of instrument results a reduction of spatial resolution. In data analysis of Feicheng flight, we use binning of 10 pixels in across-track direction, resulting in a ground pixel size of about 25×22 m^2.

Since the wavelength-to-pixel registration and the slit function shape of UVHIS could change compared to laboratory calibration results, in-flight wavelength calibration is essential for the next DOAS analysis. This in-flight wavelength calibration is achieved by fitting the measured spectra to a high-resolution solar reference (Chance and Kurucz, 2010) with slit function convolution and wavelength shift. The nominal wavelength-to-pixel registration determined in laboratory calibration, is used as initial values in the iteratively fitting procedure for convergence to the optimal solution. The effective shifts and FWHMs of different across-track position are plotted in Fig. 5. Results at three wavelengths are shown: blue for 430 nm (the start of the analysis wavelength region), green for 450 nm (the middle of the analysis wavelength region) and red for 470 nm (the end of the analysis wavelength region).

4.2 DOAS analysis

After preprocessing, the observed UVHIS spectra are analysed by the application of QDOAS (Danckaert et al., 2020) software in order to retrieve NO_2 slant column densities. The basic idea of the DOAS approach is to separate broadband signals like surface reflectance and Rayleigh scattering, and narrow-band signals like trace gas molecular absorption. The fitting window is within 430 and 470 nm wavelength region, considered to contain strongly structured NO_2 absorption features, and with low interference of other trace gases such as O_3, O_4, and water vapor. Absorption cross-sections of NO_2 and other trace gases and a synthetic Ring spectrum are simultaneously fitted to the logarithm of the ratio of the observed spectrum and a reference spectrum. These cross sections are made by convolving the high-resolution cross sections with in-flight wavelength calibration results for all across-track positions. Further details of the DOAS analysis setting can be found in Table 3.

For each analysed spectrum, the direct result of the DOAS fit is differential slant column density (dSCD), which is the difference of NO_2 integrated concentration along the effective light path between the studied spectrum and the selected reference spectrum (SCD_{ref}). Reference spectra were acquired over a clean rural area upwind of the urban and factory areas, in the lower left corner of Fig. 4. In the quite homogeneous background area, several spectra were averaged to increase the SNR of the reference spectrum. For the purpose of avoiding across-track biases, a reference spectrum is required for each across-track position because of its intrinsic spectral response. Under the assumption that the spatial and temporal variability of the stratospheric NO_2 field is negligible during the test flight, this approach eliminates the stratospheric NO_2 contribution, making the results only sensitive to the tropospheric portion. According toTROPOMI tropospheric NO_2 product of reference area on the same day, the residual NO_2 amount in the background spectra is estimated to be 3×10^{15} molec cm^{-2}.

A sample NO_2 DOAS fit result and corresponding residual of UVHIS spectra is illustrated in Fig. 6, with a differential slant column density (dSCD) of $4.95 \pm 0.34 \times 10^{16}$ molec cm^{-2} and a RMS on the residuals of 4.27×10^{-3}.

4.3 Air mass factor calculations

SCD is the integrated concentration along the effective light path of observation, which is strongly dependent on the viewing geometry and the properties that influence radiative transfer of light through the atmosphere. VCD is the integrated concentration along a single vertical transect from the Earth's surface to the top of the atmosphere, which is independent of changes in the light path length of SCD.

$$\mathrm{VCD_i} = \frac{\mathrm{dSCD}_i + \mathrm{SCD}_{ref}}{\mathrm{AMF}_i} = \frac{\mathrm{dSCD}_i + \mathrm{VCD}_{ref} \times \mathrm{AMF}_{ref}}{\mathrm{AMF}_i} \qquad (1)$$

As shown in Eq. (1), $dSCD_i$ from the DOAS fit can be converted to tropospheric VCD_i by dividing the AMF_i which accounts for enhancements in the light path (Solomon et al., 1987). In this study, tropospheric NO_2 AMFs have been computed using the SCIATRAN (Rozanov et al., 2014) radiative transfer model (RTM). SCIATRAN model numerically calculates AMFs

based on a priori information on the parameters that change effective light path, such as sun and viewing geometry, trace gas and aerosol vertical profiles, surface reflectance.

4.3.1 Parameters in RTM

185 (1) During the flight, viewing geometry is retrieved from the orientation information of the aircraft. Solar position defined by the solar zenith angle (SZA) and solar azimuth angle (SAA), as well as relative azimuth angle (RAA) can be calculated, based on the time information, latitude and longitude position of each observation. (2) Since the flight is performed under clear-sky condition, the effect of cloud presence can be neglected in AMF computation. (3) Surface reflectance used in AMF calculation is the product of the Landsat 8 Operational Land Imager (OLI) space-borne instrument (Barsi et al., 2014).

190 Coastal aerosol band (433 to 450 nm) is selected because its bandwidth is relatively narrow, and this band is basically inside the DOAS fitting window (Vermote et al., 2016). (4) Since no accurate trace gas vertical profile is available during the flight, a well-mixed vertical distribution (box profile) of NO_2 in the PBL is assumed. However, accurate PBL height is also unavailable, a typical height of 2 km is a reasonable guess in the case of sunny summer day in mid-latitude area in China. (5) Aerosol optical Depth (AOD) information used in AMF calculation is MODIS AOD product MYD04 at 470 nm on the same

195 day with resampling for every ground UVHIS pixel (Remer et al., 2005), because neither ground-based aerosol measurement is performed, nor any AERONET station data near the flight area are available. Like the NO_2 profile, the aerosol extinction box profile is constructed from the PBL height and AOD. Single scattering albedo (SSA) is assumed to be 0.93, and asymmetry factor is assumed to be 0.68 for aerosol extinction profile, based on previous studies of typical urban/industrial aerosols (Li et al., 2018).

200 The Landsat 8 surface reflectance is retrieved through atmospheric correction, using the Second Simulation of the Satellite Signal in the Solar Spectrum Vectorial (6SV) model (Vermote et al., 1997). Since there is no overpass on the same day inside UVHIS research flight area, we choose surface reflectance product on 3 May 2018 considering the sunny weather condition and no cloud presence. The spatial resolution of Landsat is about 30 m, which is slightly larger than UVHIS. A resampling of Landsat 8 surface reflectance product based on nearest neighbour interpolation is performed for every UVHIS

205 ground pixel.

The radiative transfer equation in SCIATRAN is solved in a pseudo-spherical multiple scattering atmosphere, using the scalar discrete ordinate technique. Simulations are performed for sensor altitude of 3 km above sea level, and wavelength of the middle of the NO_2 fitting windows, i.e. 450nm. A NO_2 AMF look-up table (LUT) was computed, with different RTM

210 parameter settings provided in Table 4. For each retrieved dSCD, an AMF was linear interpolated from the LUT based on the sun geometry, viewing geometry, and surface reflectance.

4.3.2 RTM dependence study

1. AMF dependence on the surface reflectance

As shown in Fig. 7, a time series of computed AMFs are plotted for the research flight on 23 June 2018, as well as the
corresponding surface reflectance, solar zenith angles, and relative azimuth angles. Other RTM parameters used in the AMF
calculations are also provided in Fig. 7. Note that only data of nadir observations are plotted for a clearer display, and time
gaps between adjacent flight lines can be observed. Despite the greater degree of varieties in viewing and sun geometries, it
is obvious that the AMFs strongly depend on the surface reflectance. Previous studies reported in Lawrence et al. (2015),
Meier et al. (2017) and Tack et al. (2017) suggest a similar conclusion. A sensitivity test was carried out to investigate the
impact of surface reflectance on the AMF calculations, based on SCIATRAN model with varying value of surface
reflectance, and fixed value of other parameters. Results of this test are shown in Fig. 8 (a), and indicate that the relation
between surface reflectance and AMF is non-linear. Especially when surface reflectance is blow 0.1, AMF increase with
surface reflectance rapidly.

Generally speaking, the AMF should be higher in the case of a bright surface reflectance, because more sunlight is reflected
from the ground back to atmosphere and then recorded by the airborne sensor. Compared to rural areas, urban and industrial
areas usually exhibit an enhancement in value of surface reflectance and subsequently an increment of AMF. As shown in
Fig. 9, the dependency of the AMF on the surface reflectance is very strong. Also a strong variability of surface reflectance
and AMF can be observed in these areas. From Fig. 9, we can also observe several slight inconsistencies between UVHIS
measured radiance and Landsat 8 surface reflectance product, due to time offset and spatial resolution difference.

2. AMF dependence on profiles

Based on airborne UVHIS retrieval product, the horizontal distribution of NO_2 can be detected, but the vertical distribution
of NO_2 in the atmosphere is not available. The assumptions we made for profile shape of trace gas and aerosol extinction do
not consider the effective variability during research flight, which can be expected in an urban area. Focusing on the impact
of different profile shapes on the AMF computation, sensitivity tests of two different NO_2 profiles which are closer to ground
surface are performed: well-mixed NO_2 box profile of 0.5 and 1 km height. Compared to the box profile of 2 km which is
close to the height of PBL, AMFs decrease by an average of 13 % in the case of a box profile of 1.0 km, while AMFs
decrease by an average of 22 % in the case of a box profile of 0.5 km.

Depending on the relative position of aerosol and trace gas layer, the optical thickness and scattering properties, aerosols can
enhance or reduce the AMF in different ways(Meier et al., 2017). If an aerosol layer is located above the majority of the
trace gas, aerosols with high SSA have a shielding effect as less scatter light passes through the trace gas layer, leading to a
shorter light path. On the other hand, if aerosols and the trace gas are present in the same layer, aerosols can lead to multiple
scattering effects which extend the light path and result a larger AMF. According to the simulations of a well-mixed aerosol

box profile of 2 km and a pure Rayleigh atmosphere, AMFs are slightly higher (about 1 %) compared to pure Rayleigh scenario.

245   3. AMF dependence on sun and viewing geometries

As can be seen in Fig. 7, the effect of sun and viewing geometries on AMFs is very small. Based on a previous study from Tack et al. (2017), changing SZA have the greatest effect on AMFs, in comparison to other sun and viewing geometries. In this study, we also did an AMF dependence analysis on SZAs and VZAs. The SZA varies from 12.8° to 37.4° during the 3 hour research flight, while the VZA ranges from 0° to 30° in most cases. As shown in Fig. 8 (b) and (c), the changes of AMF are less than 10% and 7% respectively, when other parameters are set as mean. Generally, a larger SZA or a larger VZA could result a longer light path through the atmosphere and thus a larger AMF.

4. AMF dependence on the analysis wavelength

The dependence of AMF on analysis wavelength is shown in Fig. 9, The AMF increases with the analysis wavelength. This could be explained by Rayleigh scattering characteristics: photons at shorter wavelengths are more likely to be scattered than photons at longer wavelengths, leading to the reduced sensitivity to AMF at shorter wavelengths. In the DOAS analysis wavelength window of 430-470 nm, the increase in AMF is about 2 %.

4.4 Geo-referencing and mapping

Accurate geo referencing is essential for emission source locating and data comparison, and can be achieved with sensor position and orientation information recorded by navigation system and IMU on-board. After geo-referencing, the NO_2 VCDs are gridded to combine overlapped adjacent measurements, with a spatial resolution of 0.0003° × 0.0002°. Corresponding to 27 × 22 m^2, the grid size used is slightly larger than the effective spatial resolution of the UVHIS for the purpose of reducing the number of empty grid cells. All VCDs are assigned to a grid cell based on its centre coordinates, and several VCDs in one grid cell are unweighted averaged. The final NO_2 VCD distribution map is plotted over satellite Maps layers in QGIS 3.8 software (QGIS development team, 2020).

265   **5 Results**

The tropospheric NO_2 VCD two-dimensional distribution map is shown in Fig. 10 for the research flight on 23 June 2018. With a high performance of UVHIS in spectral and spatial resolution, Figure 10 shows fine-scale NO_2 spatial variability to resolve individual emission sources. In general, the NO_2 distribution is dominated by several exhaust plumes with enhanced NO_2 concentration in the northwest part, which share a transportation pattern from south to north consistent with the wind direction. These sources include a power plant, a steel factory, two cement factories, and several carbon factories. The largest

plume with peak values of up to 3×10^{16} molec cm^{-2}, originates from an emitter inside a steel factory (number 3 in Fig. 10). This dominant plume reaches its peak value outside at a small valley about 1 km north of the factory, and is transporting at least 9 km and seems to be continuing outside the flight region. This enhanced level of NO$_2$ may be caused by terrain factor which contributes to the accumulation of pollution gases.

Number 4 to 6 represent other emitters inside the steel factory. While the exhaust plumes originated from number 4 and 5 merge with the dominant plume, the plume from number 6 transports to north individually with a peak value of 1.4×10^{16} molec cm^{-2}. A weaker plume with peak values of 1.5×10^{16} molec cm^{-2} is also detected by UVHIS, which seems to originate from the power plant. Indicated by number 2 in Fig. 10, this power plant is less than 2 km south of the steel factory. Number 1 in Fig. 10 indicates several carbon factories, which are located on the left side of the flight area. Several plumes with peak values of 1.5×10^{16} molec cm^{-2}, gradually merge together during transportation downwind. Number 7 and Number 8 in Fig. 10 represent two different cement factories. Peak values of these two plumes are 1.5×10^{16} molec cm^{-2} and 1.4×10^{16} molec cm^{-2} respectively.

Compared to the industrial areas mentioned above, the pollution levels of the rural areas are much lower due to the lack of contributing sources, ranging from 2 to 6×10^{15} molec cm^{-2}. The urban area of Feicheng city is located on the right side of the flight area. Figure 11 is an enlarged map of UVHIS NO$_2$ observations over Feicheng city, with a color scale only extends to 7×10^{15} molec cm^{-2}. Two black lines in Fig. 11 represent the truck roads in this city. The S104 is a provincial highway that crosses Feicheng from north to south, while the S330 crosses Feicheng from east to west. Although lots of noise can be observed in Fig. 11, the NO$_2$ sources in Feicheng are mainly related to traffic and concentrated along the S104.

Due to temporal discontinuity of flight lines and dynamic characteristics of tropospheric NO$_2$ field, artefacts can be observed between adjacent flight lines. Figure 12 shows three flight lines that pass through the steel factory, at local time 13:26 (a), 13:32 (c), and 14:57 (b). Panel (a) and (b) represent flight lines that cover the same area with a 1.5 hour time gap, panel (a) and (c) represent adjacent flight lines with a 6 minutes time gap. These flight lines can be divided into three regions: region A covers no NO$_2$ source but is affected by carbon factories about 3 km away; region B covers the steel factory as dominant NO$_2$ source; region C covers no NO$_2$ source and is not affected by other sources. Compared to region B, there is a large temporal variety of NO$_2$ VCDs in region A between three flight lines. Region C is temporally consistent with relatively low NO$_2$ columns. From these observations it may be concluded that largest temporal variability could occur where there is no local NO$_2$ source but is down-wind of other sources, especially when wind direction is changing.

6 NO$_2$ VCD assessment

6.1 Uncertainty analysis

The total uncertainty on the retrieved tropospheric NO$_2$ VCDs is composed of three parts: (1) uncertainties in the retrieved dSCDs; (2) uncertainties in reference column SCD$_{ref}$; (3) uncertainties in computed AMFs. Assuming that these uncertainties

originating from independent steps are sufficiently uncorrelated, the total uncertainty of tropospheric NO$_2$ VCD can be quantified as follows:

305
$$\sigma_{\mathrm{VCD}_i} = \sqrt{\left(\frac{\sigma_{\mathrm{dSCD}_i}}{\mathrm{AMF}_i}\right)^2 + \left(\frac{\sigma_{\mathrm{SCD}_{ref}}}{\mathrm{AMF}_i}\right)^2 + \left(\frac{\mathrm{SCD}_i}{\mathrm{AMF}_i^2} \times \sigma_{\mathrm{AMF}_i}\right)^2} \qquad (2)$$

The first uncertainty source, σ_{dSCDi}, originates from DOAS fit residuals and is a direct output in QDOAS software. This dSCD uncertainty is dominated by shot noise from radiance, electronic noise from the instrument, systematic uncertainties from the cross sections and errors from wavelength calibration. In this study, spatial binning of 10 pixels is performed to reduce this DOAS fit residuals, with a mean slant error of 4.8×10^{15} molec cm^{-2}. Compared to mobile DOAS system, this
310 DOAS fit error is approximately two times larger. Unlikely situation of mobile DOAS system, it becomes a major contributor to the total uncertainty in the case of an airborne sensor, especially in a clean area.

The second uncertainty source, σ_{SCDref}, is caused by the NO$_2$ residual amount in the reference spectra. Since we use TROPOMI tropospheric NO$_2$ product of the clean reference area as background amount, the uncertainty of NO$_2$ vertical column is estimated to be 1×10^{15} molec cm^{-2} directly from TROPOMI product. Assuming a tropospheric AMF of 2.0 and a
315 tropospheric AMF over the reference spectra of 1.8, this results an uncertainty 9×10^{14} molec cm^{-2} to the tropospheric vertical column.

The third uncertainty source, σ_{AMFi}, derives from uncertainties in the parameter assumptions of radiative transfer model inputs. According to previous studies (Boersma et al., 2004; Pope et al., 2015), it is treated as systematic and depends on the surface albedo, NO$_2$ profile, aerosol parameters, and cloud fraction. (1) Since the research flight took place under cloudless
320 conditions, cloud fraction is neglected in this case. (2) Results of the dependence tests in Sect. 4.3.2 suggest that the surface albedo has the most significant effect on the AMF. According to Vermote et al. (2016), the uncertainty of LANDSAT 8 surface reflectance product of band 1 is 0.011. (3) Based on the sensitivity study performed in Sect. 4.3.2, the uncertainty related to the a priori NO$_2$ profile shape is lower than 22 %. (4) According to the performed simulations of a pure Rayleigh atmosphere, the uncertainty related to aerosol state is estimated to be less than 1 %. (5) Because of the high accuracy of the
325 viewing and sun geometry, and its low impact on the AMF computation revealed in the previous section, the uncertainty related to viewing and sun geometry is expected to be ignorable. Therefore, combining all uncertainty sources in quadrature, a mean relative uncertainty of 24 % on the σ_{AMFi} is obtained.

Based on above discussion, the total uncertainties on the retrieved tropospheric NO$_2$ VCDs of all observations of the research flight are calculated. They typically range between 1.5 and 5.9×10^{15} molec cm^{-2}, with a mean value of 3.0×10^{15} molec
330 cm^{-2}.

6.2 Comparison to mobile DOAS measurements

In order to compare UVHIS NO_2 VCDs to ground-based measurements, mobile DOAS observations were performed on 23 June 2018 as well. This mobile DOAS system is composed of a spectrum acquisition unit and a GPS module. The spectrum collection unit consists of a spectrometer, a telescope, an optical fiber, and a workbench. The FOV of this telescope is 0.3°, and its focal length is 69 mm. The spectrometer used is a Maya 2000 Pro spectrometer, with a wavelength range of 290-420 nm and a spectral resolution of 0.55 nm. Zenith-sky observations of mobile DOAS are adopted for minimal blocking of buildings and trees in this research. The important properties of the mobile DOAS system and its NO_2 retrieval approach are shown in Table 5.

For better comparison with UVHIS NO_2 observations, assumptions and parameters in tropospheric NO_2 retrieval method for the mobile DOAS were set to the same as the UVHIS. For example, residual amount of NO_2 in reference spectra was set to 3×10^{15} molec cm^{-2} with an error of 1×10^{15} molec cm^{-2}; mobile DOAS observations only focus on tropospheric portion of NO_2 columns, assumed that the difference of the stratospheric NO_2 columns between observed spectra and reference spectra is negligible; vertical profiles of NO_2 and aerosol extinction, albedo, and aerosol properties in the AMF calculation were set to the same as UVHIS.

Like the uncertainty analysis of UVHIS NO_2 columns, the total uncertainty on the retrieved mobile tropospheric VCD is composed of three parts: (1) the mean uncertainty on dSCD of mobile DOAS is 1.4×10^{15} molec cm^{-2}; (2) the uncertainty of reference vertical column is estimated to be 1×10^{15} molec cm^{-2}. In the case that the tropospheric AMFs of measured and reference spectra are very close, this part results an uncertainty 1×10^{15} molec cm^{-2} to the total uncertainty; (3) the mean relative uncertainty on the AMF calculation is 22 % by square root of the quadratic sum of individual uncertainties like UVHIS. Combining these uncertainties together, the mean total uncertainties on the retrieved tropospheric NO_2 VCD is 2.1×10^{15} molec cm^{-2}.

Basically, the route of the mobile DOAS was designed to encircle the power plant and steel factory which are supposed to be predominant sources. For the comparison, mobile DOAS observations are first gridded to the same sampling of UVHIS pixels, then the VCD of UVHIS NO_2 results is extracted for each co-located mobile measurement. An overview of the mobile DOAS measurements over UVHIS NO_2 layer is shown in Fig. 13. NO_2 distributions of mobile DOAS system and UVHIS exhibit similar spatial characteristics, which low values are located in the south of the steel factory and power plant, and high values are inside the plumes.

Figure 14 (a) shows scatter plots with VCDs retrieved by UVHIS on the x-axis and mobile DOAS VCDs on the y-axis, for all co-located measurements. The corresponding results of linear regression analysis are also provided in Fig.14 (a), with a correlation coefficient of 0.69, a slope of 1.30, and an intercept of -9.01 $\times$ 10^{14}. The absolute time offset between mobile DOAS and airborne observations can be up to 1 hour, which means that both instruments cannot sample the NO_2 column at certain geolocation simultaneously. As shown in Fig. 14 (b), when only comparing UVHIS VCDs to mobile measurements

that circled the steel factory, the correlation coefficient improves to 0.86. In this case, all mobile measurements occurred inside the swath of one flight line of aircraft, and the time offset between instruments shortened to 15 minutes. In general, an underestimation of UVHIS VCDs of increased value can be observed in Fig 14 (a) and (b). Considering the variability in local emissions and meteorology, it is reasonable that the differences between these two instruments exist. Besides, the averaging effect of the area inside an UVHIS pixel can also lead to the underestimation of UVHIS compared to mobile DOAS system.

7 Conclusions

In this paper, we present the newly developed Ultraviolet Visible Hyperspectral Imaging Spectrometer (UVHIS), with a broad spectral region from 200 to 500 nm, and a high spectral resolution better than 0.5 nm. The instrument is operated in three channels at wavelength 200 to 276 nm (channel 1), 276 to 380 nm (channel 2), and 380 to 500 nm (channel 3) for minimal stray light effects and highest spectral performance. The optical design of each channel consists of a fore-optics with a FOV of 40°, an Offner imaging spectrometer, and a CCD array detector of 1032×1072 pixels.

Also we present the first tropospheric NO_2 retrieval results from the UVHIS airborne observation in June 2018. The research flight above Feicheng, China, covered an area of about 20×30 km^2 within 3 hour, with a high spatial resolution about 25×22 m^2. We first retrieve the differential NO_2 slant column densities from nadir observed spectra by application of DOAS technique, to a mean reference spectra over a clean area. Then we convert those NO_2 slant columns to tropospheric vertical columns using air mass factors derived from SCIATRAN model with Landsat 8 surface reflectance product. Total uncertainties of tropospheric NO_2 vertical columns are in range of 1.5 to 5.9×10^{15} molec cm^{-2}, with a mean value of 3.0×10^{15} molec cm^{-2}.

The two-dimensional distribution map of tropospheric NO_2 VCD demonstrates that UVHIS is adequate for trace gas pollution monitoring over a large area in a relative short time frame. With the high spatial resolution of UVHIS, different local emission sources can be distinguished, fine-scale horizontal variability can be revealed, and trace gas emission and transmission can be understood. For the flight on 23 June 2018, NO_2 distribution is dominated by several exhaust plumes which exhibit same south to north direction of transmission, with a peak value of 3×10^{16} molec cm^{-2} in the dominant plume. Comparisons of UVHIS NO_2 vertical columns to mobile DOAS observations show good agreement overall, with a correlation coefficient of 0.65 for all co-located measurements, and a correlation coefficient of 0.86 for co-located measurements that only circled the steel factory. However, an underestimation of the high NO_2 columns of UVHIS is observed relative to the mobile DOAS measurements.

High-resolution information about the NO_2 horizontal distribution, generated from UVHIS airborne data, is unique and valuable compared to ground-based instruments and space-borne sensors. In future study, UVHIS could be applied in

validation of satellite trace gas instruments, and in connection between local point observations, air quality models, and global monitoring from space.

395

Data availability. The datasets in the present work are available from the corresponding author upon reasonable request.

Author Contributions. Conceptualization, F.S.; methodology, Y.J. and H.Z.; software, Z.C.; validation, X.Q. and D.Y.; formal analysis, L.X.; resources, K.Z.; writing—original draft preparation, L.X.; writing—review and editing, F.S.

400

Competing Interest. The authors declare no conflict of interest.

Acknowledgments. We would like to thank Thomas Danckaert, Caroline Fayt and Michel Van Roozendael for help on QDOAS software.

405 *Financial support*. This research was supported by grants from the National Key Research and Development Program of China (Nos. 2016YFC0200402, 2019YFC0214702).

References

An, Z., Huang, R.-J., Zhang, R., Tie, X., Li, G., Cao, J., Zhou, W., Shi, Z., Han, Y., Gu, Z. and Ji, Y.: Severe haze in northern China: A synergy of anthropogenic emissions and atmospheric processes, Proc. Natl. Acad. Sci., 116(18), 8657–
410 8666, doi:10.1073/pnas.1900125116, 2019.

Barsi, J., Schott, J., Hook, S., Raqueno, N., Markham, B. and Radocinski, R.: Landsat-8 Thermal Infrared Sensor (TIRS) Vicarious Radiometric Calibration, Remote Sens., 6(11), 11607–11626, doi:10.3390/rs61111607, 2014.

Boersma, K. F., Eskes, H. J. and Brinksma, E. J.: Error analysis for tropospheric NO_2 retrieval from space, J. Geophys. Res. Atmospheres, 109(D4), doi:10.1029/2003JD003962, 2004.

415 Bovensmann, H., Burrows, J. P., Buchwitz, M. and Frerick, J.: SCIAMACHY: Mission Objectives and Measurement Modes, J. ATMOSPHERIC Sci., 56, 24, 1999.

Burrows, J. P., Weber, M., Buchwitz, M., Rozanov, V., TTER-WEIßENMAYER, A. L., Richter, A., Bramstedt, K., Eichmann, K.-U., Eisinger, M. and Perner, D.: The Global Ozone Monitoring Experiment (GOME): Mission Concept and First Scientific Results, J. ATMOSPHERIC Sci., 56, 25, 1999.

420 Chance, K. and Kurucz, R. L.: An improved high-resolution solar reference spectrum for earth's atmosphere measurements in the ultraviolet, visible, and near infrared, J. Quant. Spectrosc. Radiat. Transf., 111(9), 1289–1295, doi:10.1016/j.jqsrt.2010.01.036, 2010.

Chance, K. V. and Spurr, R. J. D.: Ring effect studies: Rayleigh scattering, including molecular parameters for rotational Raman scattering, and the Fraunhofer spectrum, Appl. Opt., 36(21), 5224, doi:10.1364/AO.36.005224, 1997.

425 Cheng, L., Tao, J., Valks, P., Yu, C., Liu, S., Wang, Y., Xiong, X., Wang, Z. and Chen, L.: NO_2 Retrieval from the Environmental Trace Gases Monitoring Instrument (EMI): Preliminary Results and Intercomparison with OMI and TROPOMI, Remote Sens., 11(24), 3017, doi:10.3390/rs11243017, 2019.

Crippa, M., Guizzardi, D., Muntean, M., Schaaf, E., Dentener, F., van Aardenne, J. A., Monni, S., Doering, U., Olivier, J. G. J., Pagliari, V. and Janssens-Maenhout, G.: Gridded Emissions of Air Pollutants for the period 1970–2012 within EDGAR
430 v4.3.2, preprint, Data, Algorithms, and Models., 2018.

Danckaert, T., Fayt, C., Roozendael, M. V., Smedt, I. D., Letocart, V., Merlaud, A. and Pinardi, G.: QDOAS Software user manual, [online] Available from: http://uv-vis.aeronomie.be/software/QDOAS/QDOAS_manual.pdf (Accessed 2 June 2020), 2020.

Heue, K.-P., Wagner, T., Broccardo, S. P., Walter, D., Piketh, S. J., Ross, K. E., Beirle, S. and Platt, U.: Direct observation
435 of two dimensional trace gas distributions with an airborne Imaging DOAS instrument, Atmospheric Chem. Phys., 8(22), 6707–6717, doi:10.5194/acp-8-6707-2008, 2008.

Lawrence, J. P., Anand, J. S., Vande Hey, J. D., White, J., Leigh, R. R., Monks, P. S. and Leigh, R. J.: High-resolution measurements from the airborne Atmospheric Nitrogen Dioxide Imager (ANDI), Atmospheric Meas. Tech., 8(11), 4735–4754, doi:10.5194/amt-8-4735-2015, 2015.

440 Levelt, P. F., van den Oord, G. H. J., Dobber, M. R., Malkki, A., Huib Visser, Johan de Vries, Stammes, P., Lundell, J. O. V. and Saari, H.: The ozone monitoring instrument, IEEE Trans. Geosci. Remote Sens., 44(5), 1093–1101, doi:10.1109/TGRS.2006.872333, 2006.

Li, Z. Q., Xu, H., Li, K. T., Li, D. H., Xie, Y. S., Li, L., Zhang, Y., Gu, X. F., Zhao, W., Tian, Q. J., Deng, R. R., Su, X. L., Huang, B., Qiao, Y. L., Cui, W. Y., Hu, Y., Gong, C. L., Wang, Y. Q., Wang, X. F., Wang, J. P., Du, W. B., Pan, Z. Q., Li,
445 Z. Z. and Bu, D.: Comprehensive Study of Optical, Physical, Chemical, and Radiative Properties of Total Columnar Atmospheric Aerosols over China: An Overview of Sun–Sky Radiometer Observation Network (SONET) Measurements, Bull. Am. Meteorol. Soc., 99(4), 739–755, doi:10.1175/BAMS-D-17-0133.1, 2018.

Liu, F., Beirle, S., Zhang, Q., van der A, R. J., Zheng, B., Tong, D. and He, K.: NO_x emission trends over Chinese cities estimated from OMI observations during 2005 to 2015, Atmospheric Chem. Phys., 17(15), 9261–9275, doi:10.5194/acp-17-
450 9261-2017, 2017.

Liu, J., Si, F., Zhou, H., Zhao, M., Dou, K., Wang, Y. and Liu, W.: Observation of two-dimensional distributions of NO_2 with airborne imaging DOAS technology, Acta Phys. Sin., 64(3), 034217, doi:10.7498/aps.64.034217, 2015.

Meier, A. C., Schönhardt, A., Bösch, T., Richter, A., Seyler, A., Ruhtz, T., Constantin, D.-E., Shaiganfar, R., Wagner, T., Merlaud, A., Van Roozendael, M., Belegante, L., Nicolae, D., Georgescu, L. and Burrows, J. P.: High-resolution airborne
455 imaging DOAS measurements of NO_2 above Bucharest during AROMAT, Atmospheric Meas. Tech., 10(5), 1831–1857, doi:10.5194/amt-10-1831-2017, 2017.

Munro, R., Lang, R., Klaes, D., Poli, G., Retscher, C., Lindstrot, R., Huckle, R., Lacan, A., Grzegorski, M., Holdak, A., Kokhanovsky, A., Livschitz, J. and Eisinger, M.: The GOME-2 instrument on the Metop series of satellites: instrument design, calibration, and level 1 data processing – an overview, Atmospheric Meas. Tech., 9(3), 1279–1301, doi:10.5194/amt-
460 9-1279-2016, 2016.

Platt, U. and Stutz, J.: Differential Optical Absorption Spectroscopy: Principles and Applications, Springer-Verlag, Berlin, Germany., 2008.

Pope, R. J., Chipperfield, M. P., Savage, N. H., Ordóñez, C., Neal, L. S., Lee, L. A., Dhomse, S. S., Richards, N. A. D. and Keslake, T. D.: Evaluation of a regional air quality model using satellite column NO_2 treatment of observation errors and model boundary conditions and emissions, Atmospheric Chem. Phys., 15(10), 5611–5626, doi:10.5194/acp-15-5611-2015, 2015.

Popp, C., Brunner, D., Damm, A., Van Roozendael, M., Fayt, C. and Buchmann, B.: High-resolution NO_2 remote sensing from the Airborne Prism EXperiment (APEX) imaging spectrometer, Atmospheric Meas. Tech., 5(9), 2211–2225, doi:10.5194/amt-5-2211-2012, 2012.

QGIS development team: QGIS Geographic Information System, Open Source Geospatial Foundation, QGIS Geogr. Inf. Syst. Open Source Geospatial Found. [online] Available from: https://www.qgis.org/en/site/ (Accessed 2 June 2020), 2020.

Remer, L. A., Kaufman, Y. J., Tanré, D., Mattoo, S., Chu, D. A., Martins, J. V., Li, R.-R., Ichoku, C., Levy, R. C., Kleidman, R. G., Eck, T. F., Vermote, E. and Holben, B. N.: The MODIS Aerosol Algorithm, Products, and Validation, J. Atmospheric Sci., 62(4), 947–973, doi:10.1175/JAS3385.1, 2005.

Rothman, L. S., Gordon, I. E., Babikov, Y., Barbe, A., Chris Benner, D., Bernath, P. F., Birk, M., Bizzocchi, L., Boudon, V., Brown, L. R., Campargue, A., Chance, K., Cohen, E. A., Coudert, L. H., Devi, V. M., Drouin, B. J., Fayt, A., Flaud, J.-M., Gamache, R. R., Harrison, J. J., Hartmann, J.-M., Hill, C., Hodges, J. T., Jacquemart, D., Jolly, A., Lamouroux, J., Le Roy, R. J., Li, G., Long, D. A., Lyulin, O. M., Mackie, C. J., Massie, S. T., Mikhailenko, S., Müller, H. S. P., Naumenko, O. V., Nikitin, A. V., Orphal, J., Perevalov, V., Perrin, A., Polovtseva, E. R., Richard, C., Smith, M. A. H., Starikova, E., Sung, K., Tashkun, S., Tennyson, J., Toon, G. C., Tyuterev, Vl. G. and Wagner, G.: The HITRAN2012 molecular spectroscopic database, J. Quant. Spectrosc. Radiat. Transf., 130, 4–50, doi:10.1016/j.jqsrt.2013.07.002, 2013.

Rozanov, V. V., Rozanov, A. V., Kokhanovsky, A. A. and Burrows, J. P.: Radiative transfer through terrestrial atmosphere and ocean: Software package SCIATRAN, J. Quant. Spectrosc. Radiat. Transf., 133, 13–71, doi:10.1016/j.jqsrt.2013.07.004, 2014.

Seinfeld, J. H. and Pandis, S. N.: Atmospheric chemistry and physics: from air pollution to climate change, Third edition., John Wiley & Sons, Hoboken, New Jersey., 2016.

Serdyuchenko, A., Gorshelev, V., Weber, M., Chehade, W. and Burrows, J. P.: High spectral resolution ozone absorption cross-sections - Part 2: Temperature dependence, Atmospheric Meas. Tech., 7(2), 625–636, doi:10.5194/amt-7-625-2014, 2014.

Solomon, S.: Stratospheric ozone depletion: A review of concepts and history, Rev. Geophys., 37(3), 275–316, doi:10.1029/1999RG900008, 1999.

Solomon, S., Schmeltekopf, A. L. and Sanders, R. W.: On the interpretation of zenith sky absorption measurements, J. Geophys. Res., 92(D7), 8311, doi:10.1029/JD092iD07p08311, 1987.

Tack, F., Merlaud, A., Iordache, M.-D., Danckaert, T., Yu, H., Fayt, C., Meuleman, K., Deutsch, F., Fierens, F. and Van Roozendael, M.: High-resolution mapping of the NO_2 spatial distribution over Belgian urban areas based on airborne APEX remote sensing, Atmospheric Meas. Tech., 10(5), 1665–1688, doi:10.5194/amt-10-1665-2017, 2017.

Tack, F., Merlaud, A., Meier, A. C., Vlemmix, T., Ruhtz, T., Iordache, M.-D., Ge, X., van der Wal, L., Schuettemeyer, D., Ardelean, M., Calcan, A., Constantin, D., Schönhardt, A., Meuleman, K., Richter, A. and Van Roozendael, M.: Intercomparison of four airborne imaging DOAS systems for tropospheric NO_2 mapping – the AROMAPEX campaign, Atmospheric Meas. Tech., 12(1), 211–236, doi:10.5194/amt-12-211-2019, 2019.

Thalman, R. and Volkamer, R.: Temperature dependent absorption cross-sections of O_2–O_2 collision pairs between 340 and 630 nm and at atmospherically relevant pressure, Phys. Chem. Chem. Phys., 15(37), 15371, doi:10.1039/c3cp50968k, 2013.

Vandaele, A. C., Hermans, C., Simon, P. C., Carleer, M., Colin, R., Fally, S., Mérienne, M. F., Jenouvrier, A. and Coquart, B.: Measurements of the NO_2 absorption cross-section from 42 000 cm^{-1} to 10 000 cm^{-1} (238–1000 nm) at 220 K and 294 K,
505   J. Quant. Spectrosc. Radiat. Transf., 59(3–5), 171–184, doi:10.1016/S0022-4073(97)00168-4, 1998.

Veefkind, J. P., Aben, I., McMullan, K., Förster, H., de Vries, J., Otter, G., Claas, J., Eskes, H. J., de Haan, J. F., Kleipool, Q., van Weele, M., Hasekamp, O., Hoogeveen, R., Landgraf, J., Snel, R., Tol, P., Ingmann, P., Voors, R., Kruizinga, B., Vink, R., Visser, H. and Levelt, P. F.: TROPOMI on the ESA Sentinel-5 Precursor: A GMES mission for global observations of the atmospheric composition for climate, air quality and ozone layer applications, Remote Sens. Environ.,
510   120, 70–83, doi:10.1016/j.rse.2011.09.027, 2012.

Vermote, E., Justice, C., Claverie, M. and Franch, B.: Preliminary analysis of the performance of the Landsat 8/OLI land surface reflectance product, Remote Sens. Environ., 11, 2016.

Vermote, E. F., Tanre, D., Deuze, J. L., Herman, M. and Morcette, J.-J.: Second Simulation of the Satellite Signal in the Solar Spectrum, 6S: an overview, IEEE Trans. Geosci. Remote Sens., 35(3), 675–686, doi:10.1109/36.581987, 1997.

515   Zhang, C., Liu, C., Hu, Q., Cai, Z., Su, W., Xia, C., Zhu, Y., Wang, S. and Liu, J.: Satellite UV-Vis spectroscopy: implications for air quality trends and their driving forces in China during 2005–2017, Light Sci. Appl., 8(1), 100, doi:10.1038/s41377-019-0210-6, 2019.

Zhang, C., Liu, C., Chan, K. L., Hu, Q., Liu, H., Li, B., Xing, C., Tan, W., Zhou, H., Si, F. and Liu, J.: First observation of tropospheric nitrogen dioxide from the Environmental Trace Gases Monitoring Instrument onboard the GaoFen-5 satellite,
520   Light Sci. Appl., 9(1), 66, doi:10.1038/s41377-020-0306-z, 2020.

Zhang, Q., Huang, S., Zhao, X., Si, F., Zhou, H., Wang, Y. and Liu, W.: The Design and Implementation of CCD Refrigeration System of Imaging Spectrometer, Acta Photonica Sin., 46(3), 0311004, 2017.

Zhao, M. J., Si, F. Q., Zhou, H. J., Wang, S. M., Jiang, Y. and Liu, W. Q.: Preflight calibration of the Chinese Environmental Trace Gases Monitoring Instrument (EMI), Atmospheric Meas. Tech., 11(9), 5403–5419, doi:10.5194/amt-11-5403-2018,
525   2018.

530

535

Table 1: UVHIS instrument characteristics of three channels**.**

Characteristic	Channel 1	Channel 2	Channel 3
Wavelength range	200-276 nm	276-380 nm	380-500 nm
Spectral sampling	0.074 nm	0.10 nm	0.12 nm
Spectral resolution	0.34 nm	0.46 nm	0.49 nm
FOV	40°	40°	40°
Focal length	18 mm	18 mm	18 mm
Across-track angular resolution	0.5 mrad	0.5 mrad	0.5 mrad
f-number	3.4	3.6	3.6
Detector size	1032 × 1072	1032 × 1072	1032 × 1072

540

Table 2. Preflight wavelength calibration results (FWHMs) of UVHIS channel 3 for 9 viewing angles. Light sources used in the calibration are a mercury-argon lamp and a tunable laser. Slit function shapes are retrieved by least square fitting of characteristic spectral lines, using a symmetric Gaussian function.

FOV	379.887 nm	404.656 nm	450.504 nm	500.566 nm
-20°	0.35 nm	0.35 nm	0.39 nm	0.50 nm
-15°	0.33 nm	0.31 nm	0.33 nm	0.43 nm
-10°	0.31 nm	0.29 nm	0.29 nm	0.41 nm
-5°	0.31 nm	0.30 nm	0.29 nm	0.34 nm
0°	0.31 nm	0.32 nm	0.30 nm	0.30 nm
5°	0.34 nm	0.36 nm	0.34 nm	0.30 nm
10°	0.38 nm	0.39 nm	0.38 nm	0.32 nm
15°	0.40 nm	0.44 nm	0.42 nm	0.35 nm
20°	0.45 nm	0.46 nm	0.47 nm	0.38 nm

545

550

Table 3. Main analysis parameters and absorption cross sections for NO_2 DOAS retrieval.

Parameter	Settings
Wavelength calibration	Solar atlas, (Chance and Kurucz, 2010)
Fitting interval	430-470 nm
Cross sections	
NO_2	298 K, Vandaele et al. (1998)
O_3	223 K, Serdyuchenko et al. (2014)
O_4	293 K, Thalman and Volkamer (2013)
H_2O	293 K, Rothman et al. (2013)
Ring effect	Chance and Spurr (1997)
Polynomial term	Order 5
Intensity offset	Order 1

555

560 **Table 4.** Overview of the input parameters in the SCIATRAN RTM, characterizing the AMF LUT.

RTM Parameter	Grid settings
Wavelength	450 nm
Sensor altitude	3 km
Surface reflectance	0.01-0.4 (steps of 0.01)
Solar zenith angle	10-40° (steps of 10°)
Viewing zenith angle	0-40° (steps of 10°)
Relative azimuth angle	0-180° (steps of 30°)
Aerosol optical depth	0-1 (steps of 0.1)
Aerosol extinction profile	Box of 2.0 km
NO_2 profile	Box of 2.0 km

565

Table 5. Properties of the mobile DOAS system and its NO_2 fit.

Parameter	Settings
Elevation angle	zenith
Fitting interval	356-376 nm
Wavelength calibration	Mercury lamp
Cross sections	
NO_2	298 K, Vandaele et al. (1998)
O_3	223 K, Serdyuchenko et al. (2014)
O_4	293 K, Thalman and Volkamer (2013)
Ring effect	Chance and Spurr (1997)
Polynomial term	Order 5
Intensity offset	Order 1

570

575

580

585

1. Telecentric fore-optics
2. Filter and slit
3. Concave mirror
4. Convex grating
5. CCD
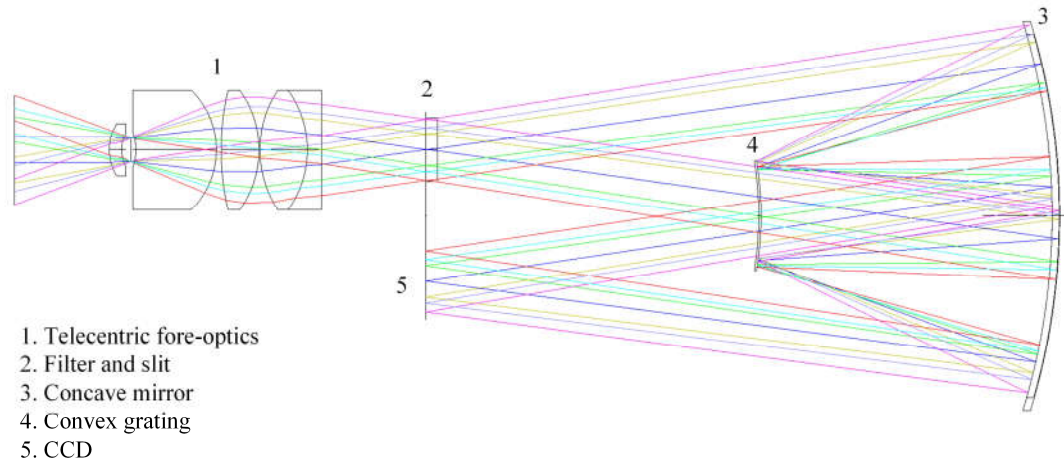
Figure 1. Optical layout of the UVHIS channel 3. Optical design of channel 1 and channel 2 is similar.

590

595

600

605
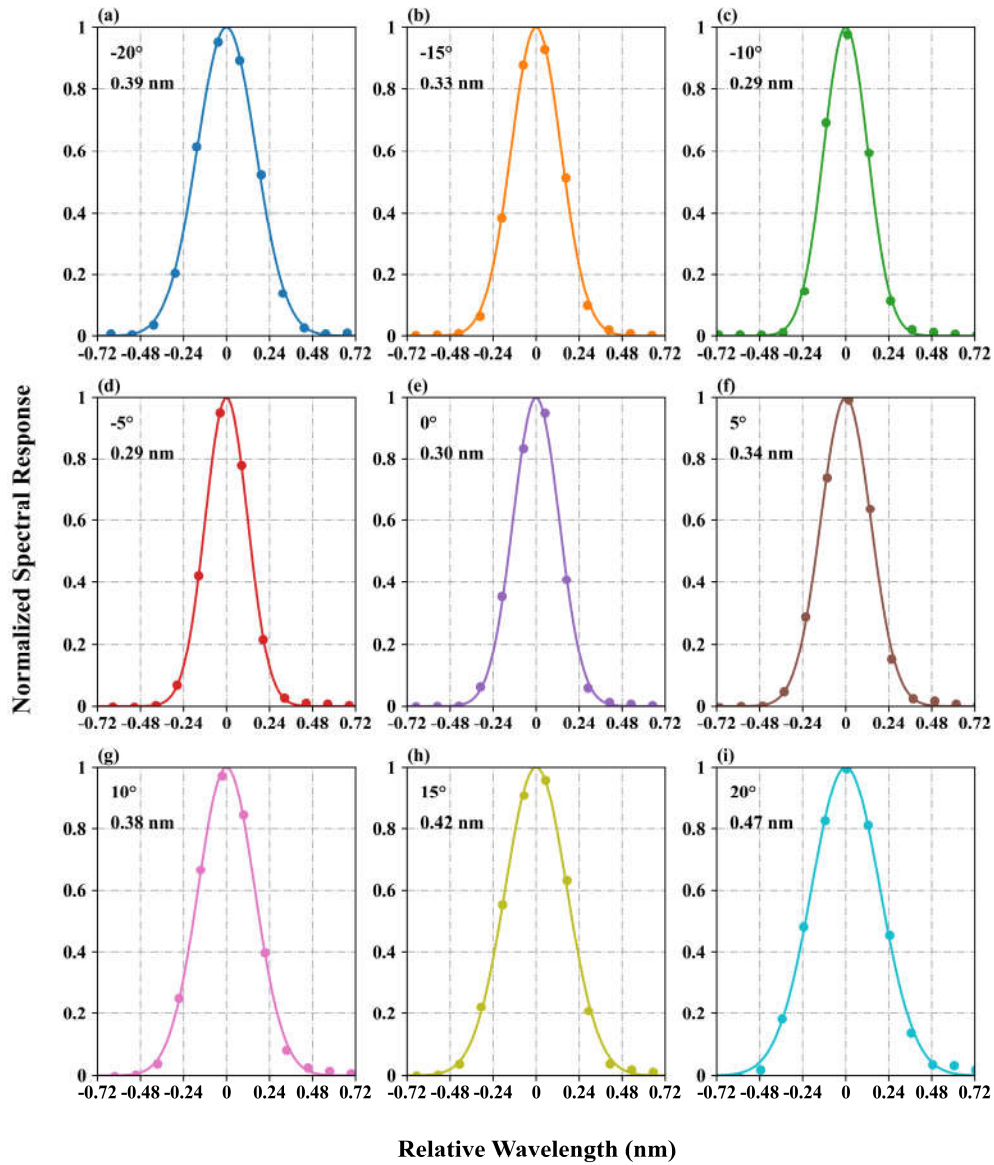
610   **Figure 2.** Measured slit functions (dots) at 450.504 nm and retrieved slit function shapes (lines) using a symmetric Gaussian function for 9 viewing angles.
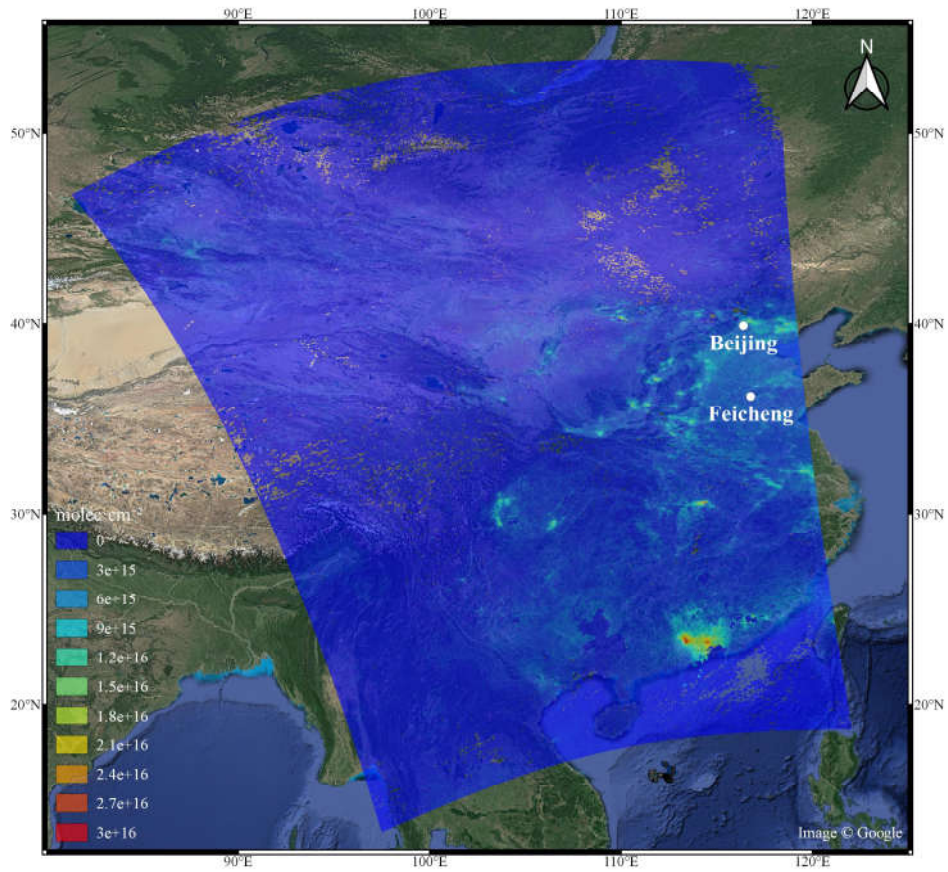
Figure 3. TROPOMI observation of tropospheric NO₂ over China on 23 June, 2018. The location of UVHIS flight (Feicheng city) is also plotted in the map.

615
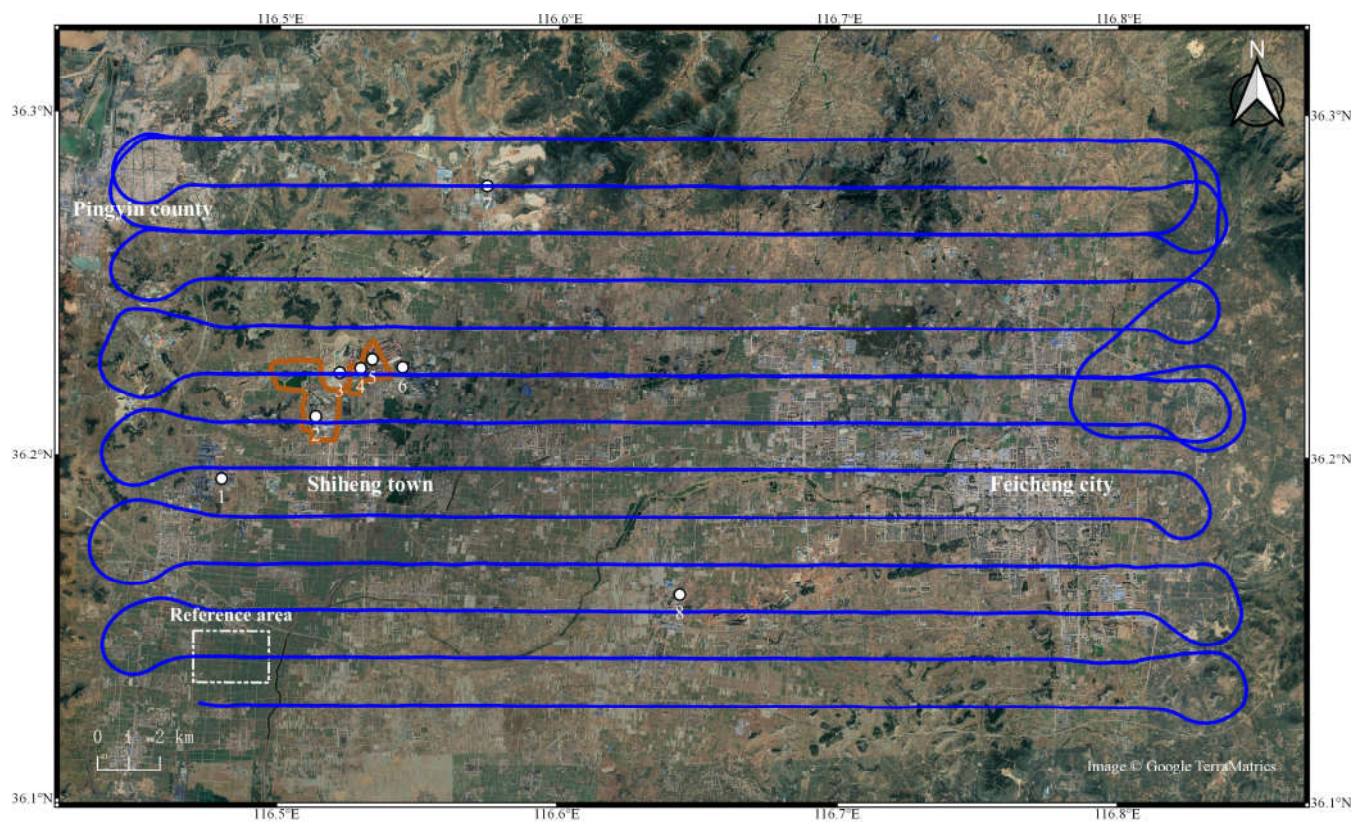
Figure 4. Overview of the Feicheng demonstration flight on 23 June, 2018. Flight lines are shown in blue. Two orange circles represent the routes of mobile DOAS system. White dots numbered from 1 to 8 represent the major emission sources. Number 1: several carbon factories; number 2: a power plant; number 3-6: individual emitters inside the steel factories, while number 4 and 5 are inside the circle of one mobile DOAS route; number 7-8: two cement factories. White dashed box represents the reference area.
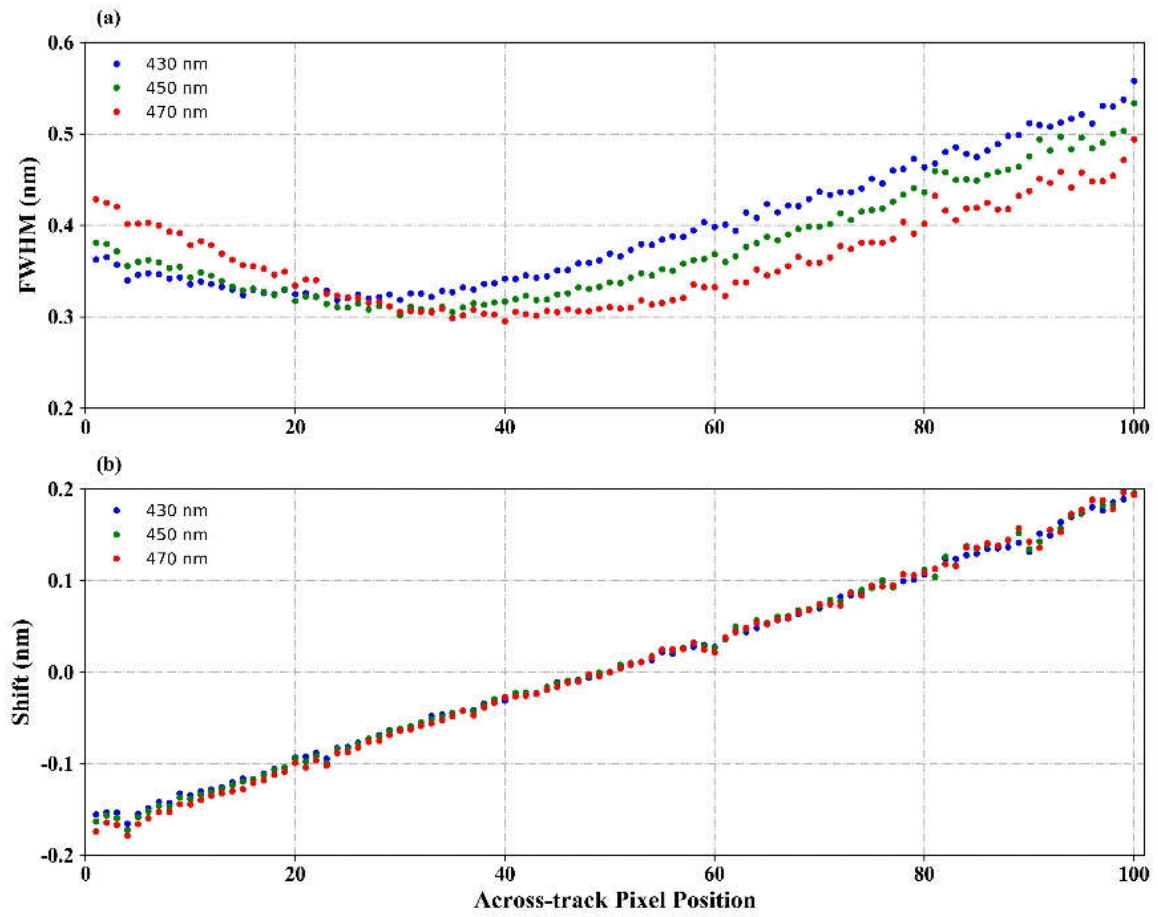
Figure 5. In-flight spectral calibration: (**a**) the spectral resolution (FWHM); (**b**) the spectral shift on different across-track position. Results at three wavelengths are plotted: blue for 430 nm, green for 450 nm and red for 470 nm.

625
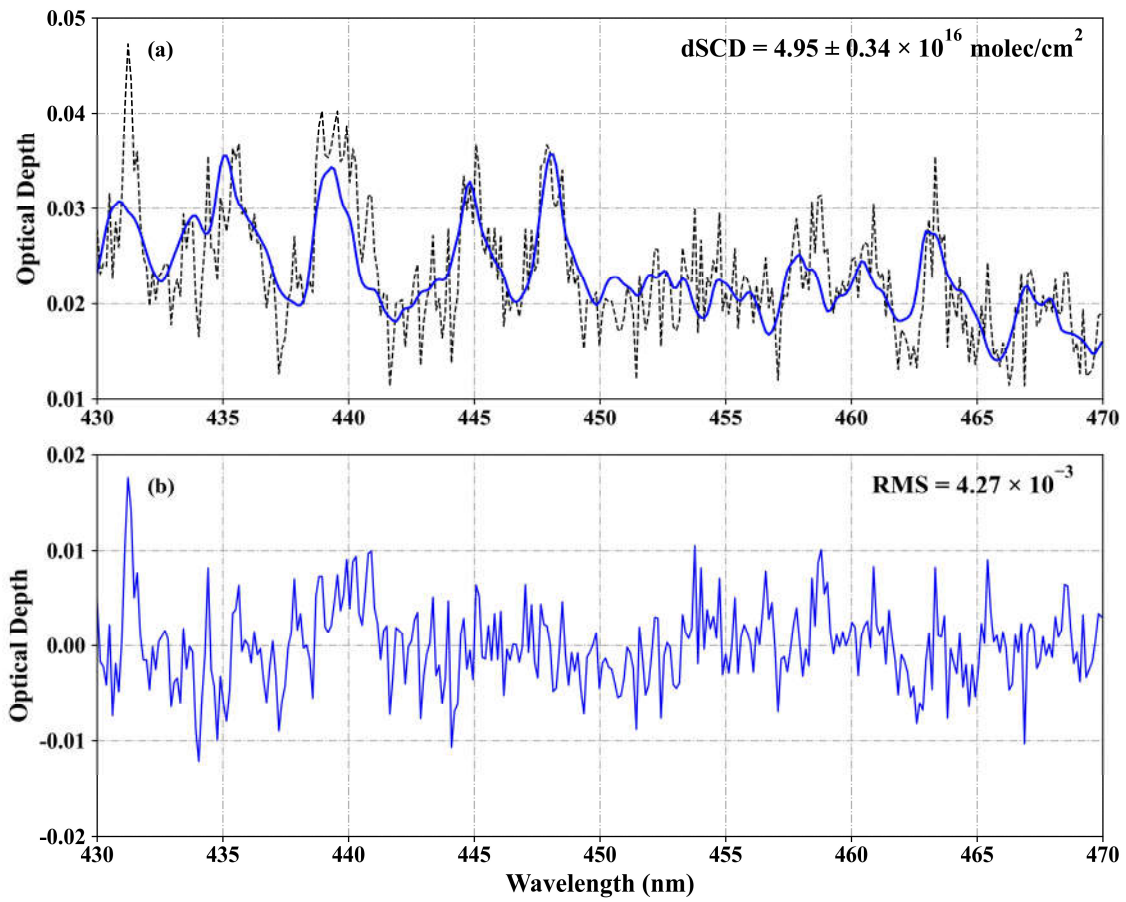
Figure 6. Sample DOAS fit result for NO_2: (**a**) observed (black dashed line) and fitted (blue line) optical depths from measured spectra; (**b**) the remaining residuals of DOAS fit.

630
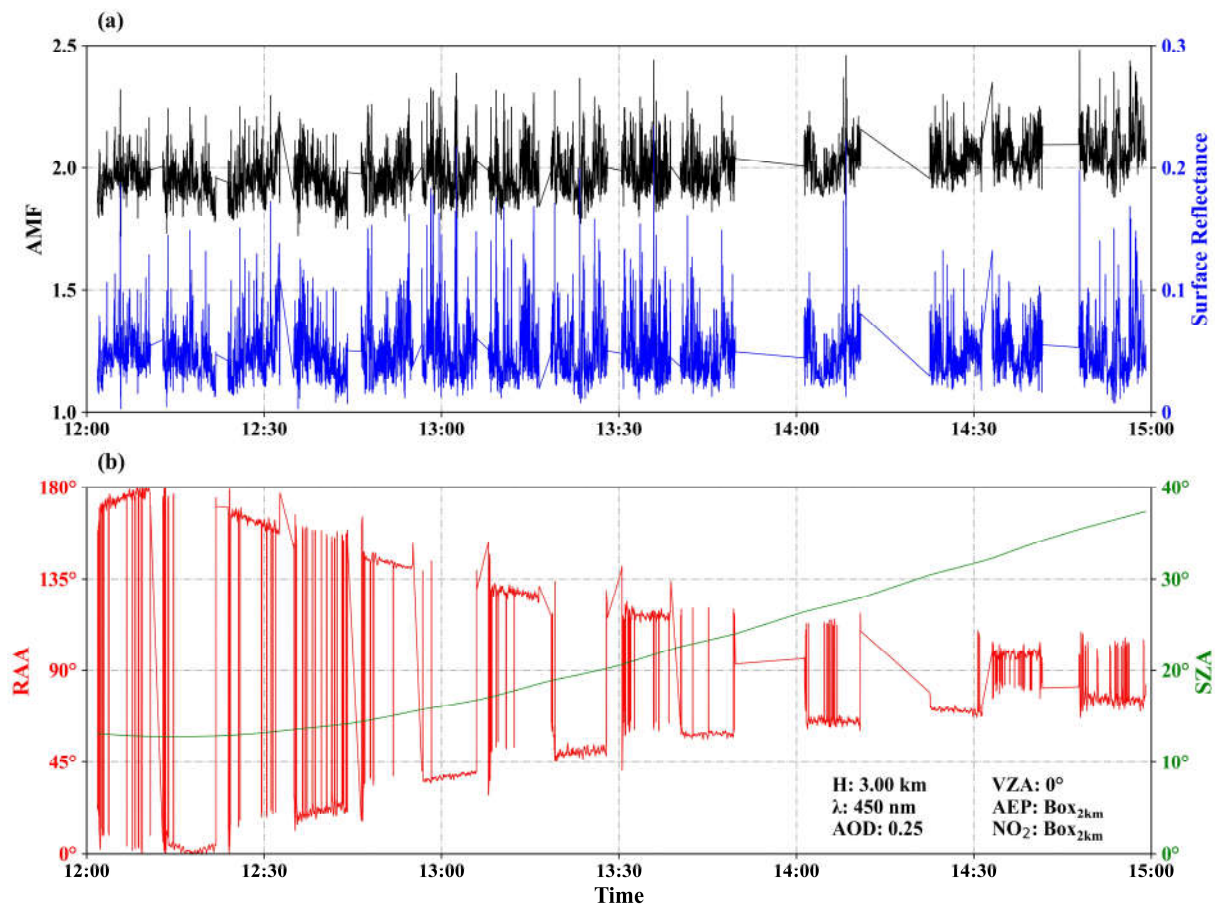
Figure 7. Time series of NO₂ AMF compared with **(a)** surface reflectance; **(b)** SZA and RAA for the research flight on 23 June 2018, computed with SCIATRAN model based on the RTM parameters from the UVHIS instrument. Only data of the nadir observations in each flight line are plotted.

640
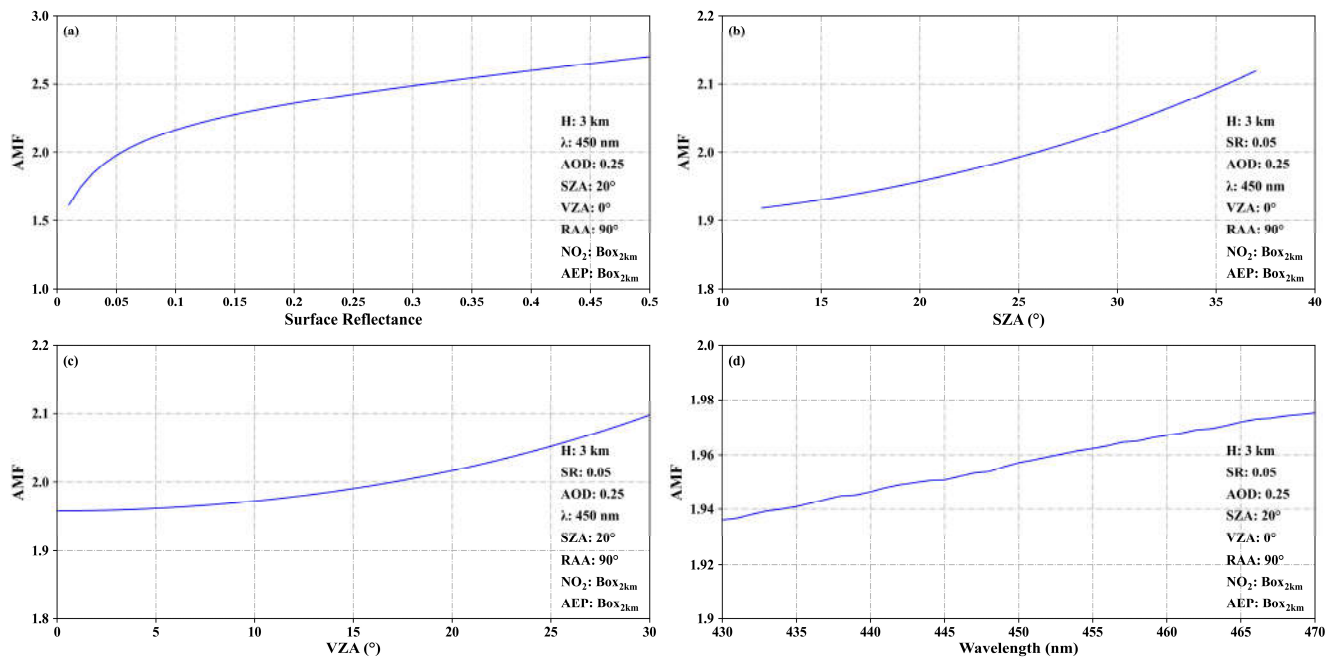
Figure 8. AMF dependence analysis results (a): on the surface reflectance; (b): on the SZAs; (c): on the VZAs; (d): on the wavelength.

645
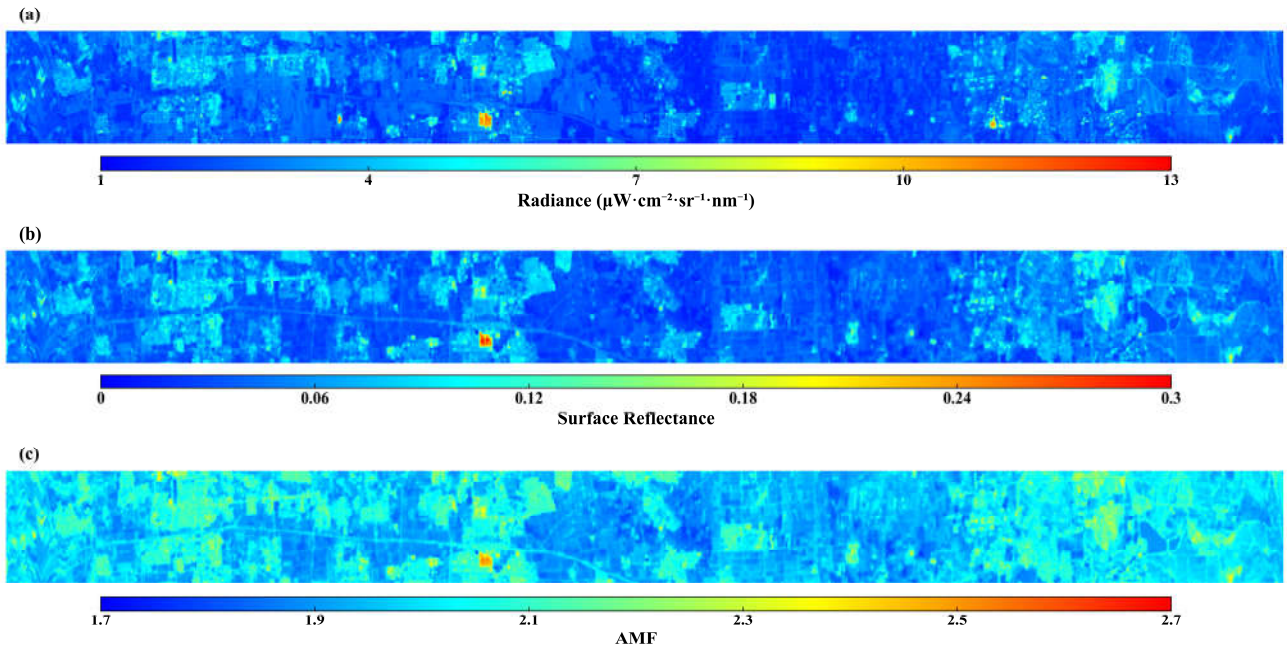
Figure 9. (a) UVHIS Measured radiance; **(b)** Landsat 8 Surface reflectance; (c) computed AMFs, for one flight line of the Feicheng data set. A strong dependency of the AMF on the surface reflectance can be observed.

650

655

660

665
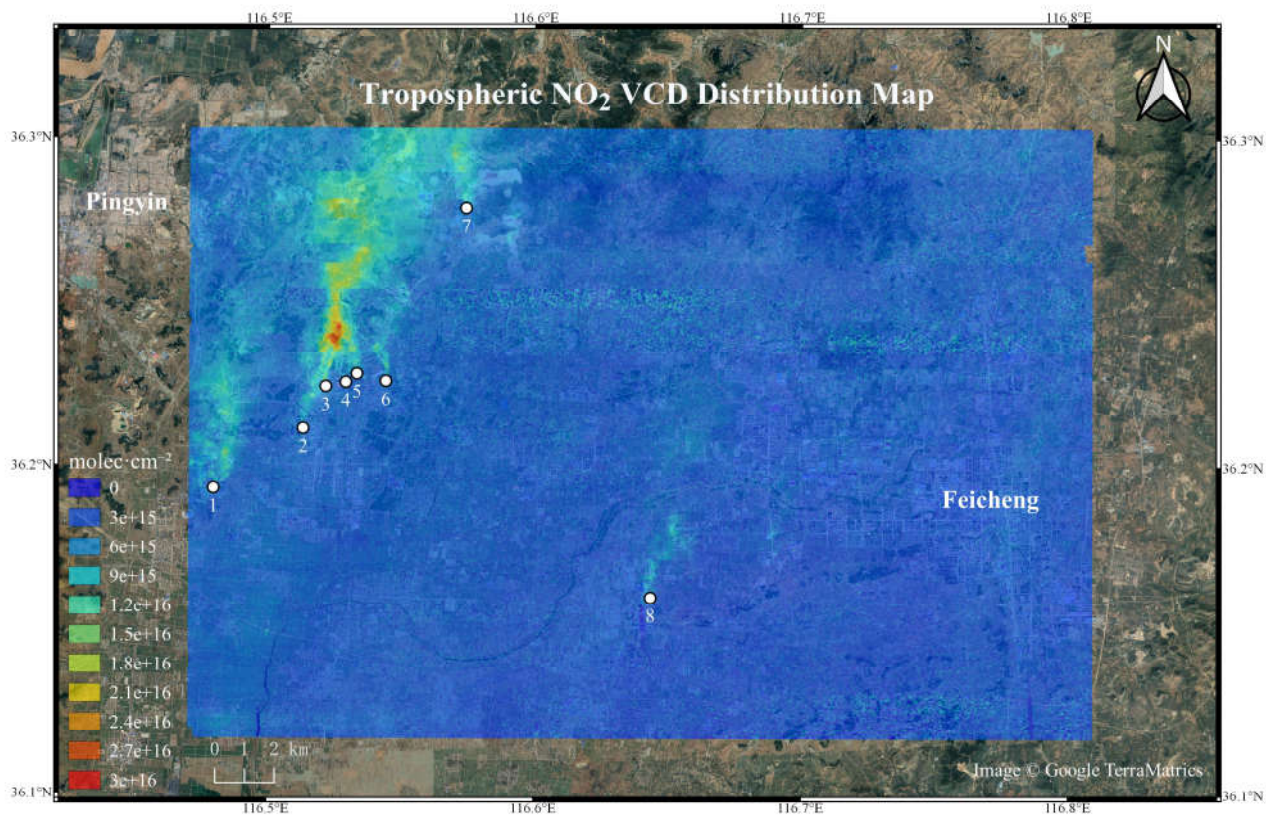
Figure 10. Tropospheric NO₂ VCD map retrieved from UVHIS over Feicheng on 23 June 2018. The major contributing NO₂ emission sources are indicated by number 1 to 8.

670
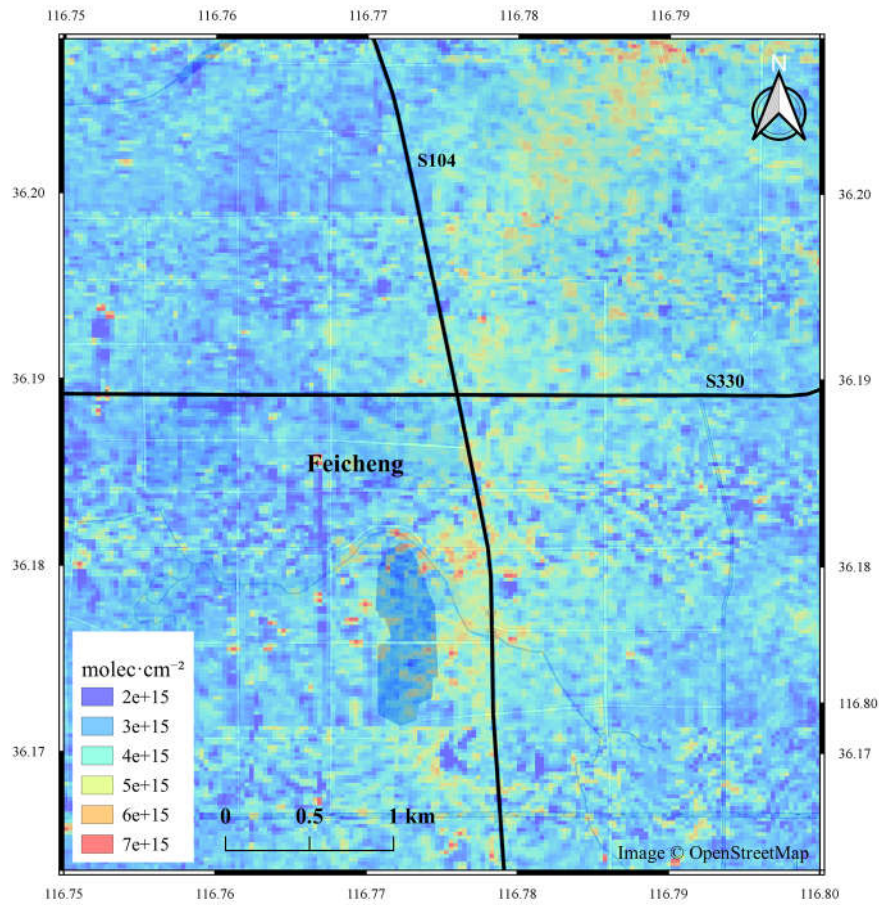
675 **Figure 11.** Enlargement of UVHIS NO$_2$ VCD map over Feicheng city with a color scale only extends to 7×10^{15} molec cm^{-2}. Two black lines in the map represent two truck roads that cross Feicheng city: S104, and S330.
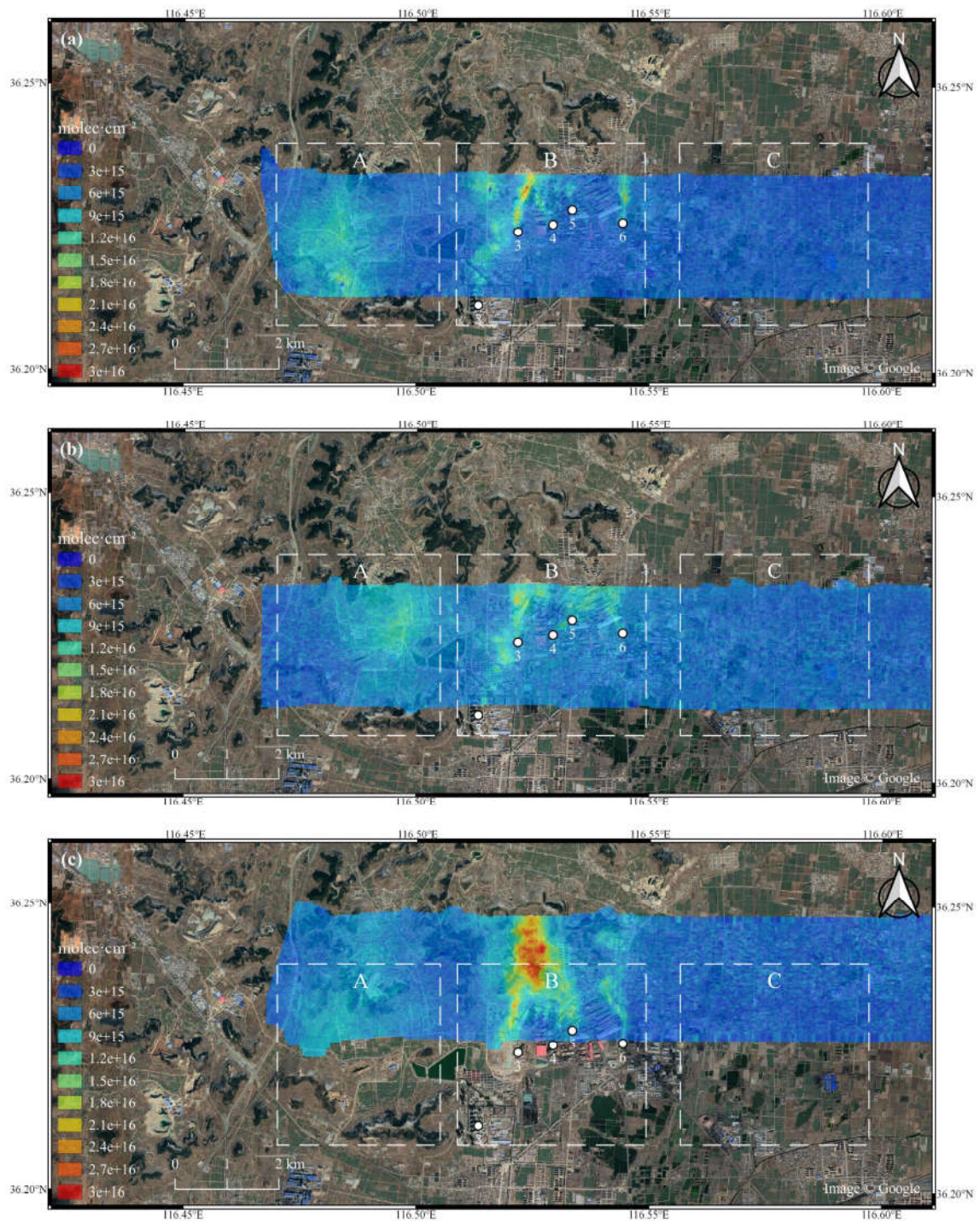
Figure 12. Three flight lines that pass through the steel factory, at local time 13:26 (a), 13:32 (c), and 14:57 (b). Panel (a) and (b) represent flight lines that cover the same area with a 1.5 hour time gap, panel (a) and (c) represent adjacent flight lines with a 6 minutes time gap.
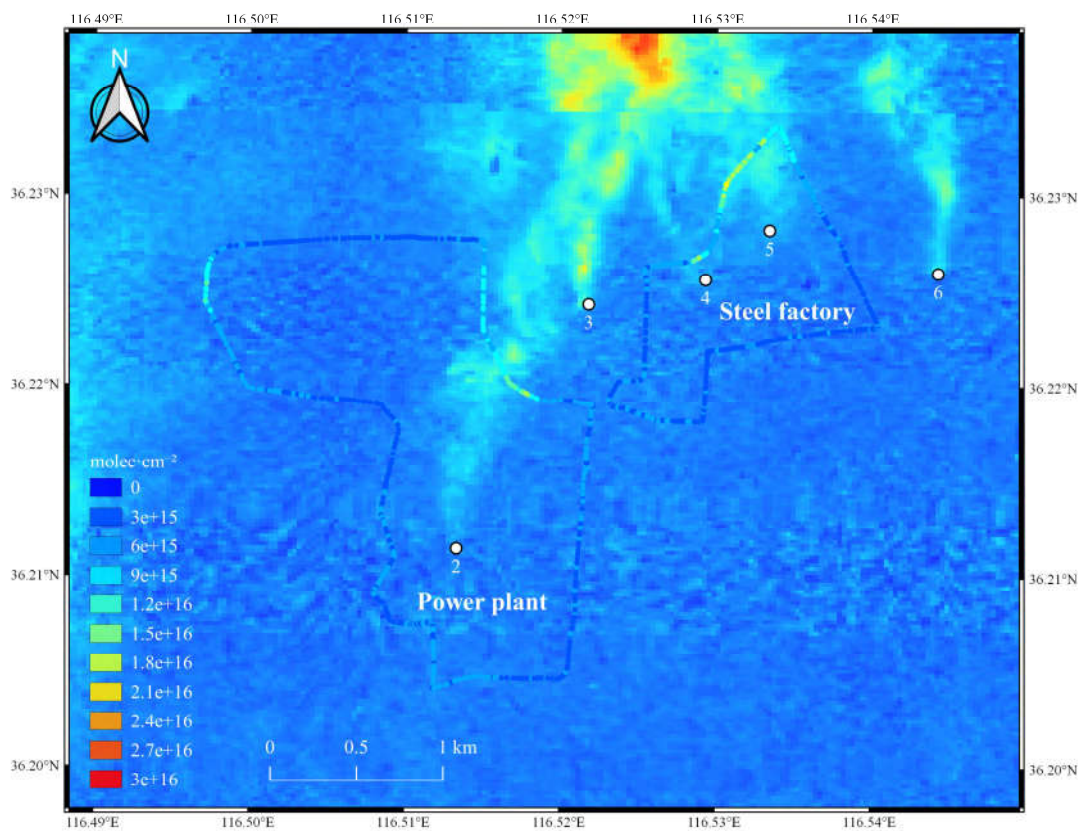
680

Figure 13. Overview of VCDs retrieved from ground-based mobile DOAS system (circle marks), and VCDs retrieved by UVHIS (background layer), measured on 23 June 2018.

685

690
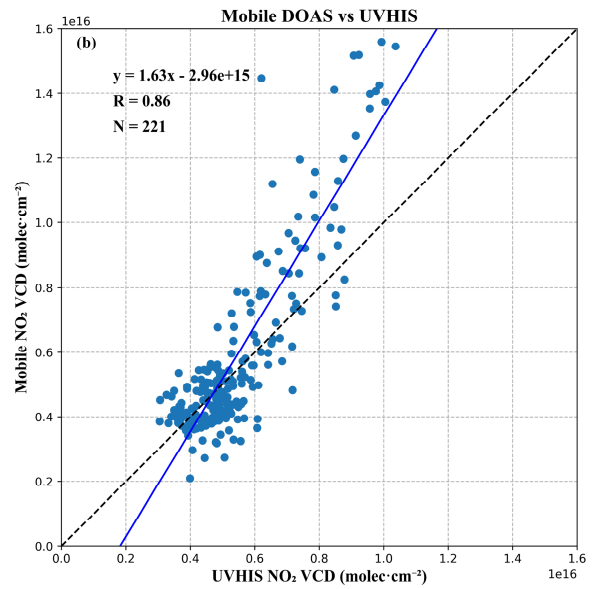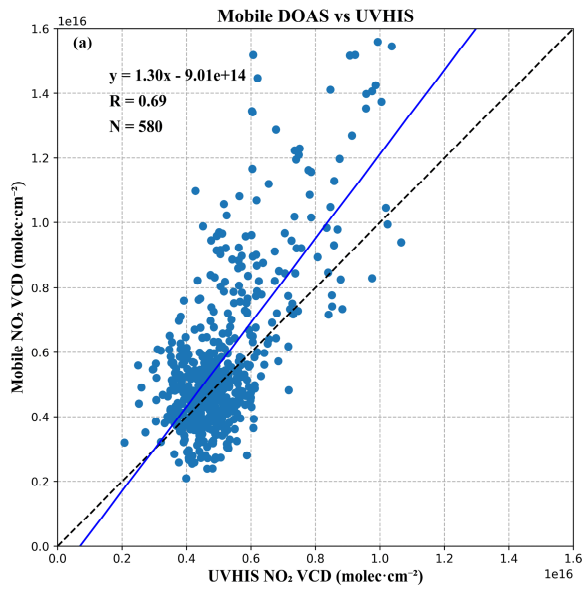
Figure 14. Scatter plot and linear regression analysis of the co-located NO$_2$ VCDs, retrieved from UVHIS and mobile DOAS system, (a) for all co-located measurements, (b) for co-located measurements that only circled the steel factory.